Dynamic morphoskeletons in development

Serra, Mattia; Streichan, Sebastian; Chuai, Manli; Weijer, Cornelis J.; Mahadevan, L.

Published in:
Proceedings of the National Academy of Sciences of the United States of America

DOI:
10.1073/pnas.1908803117

Publication date:
2020

Document Version
Peer reviewed version

PNAS
www.pnas.org

Supplementary Information for

Dynamic morphoskeletons in development

Mattia Serra, Sebastian Streichan, Manli Chuai, Cornelis J. Weijer and L. Mahadevan

Corresponding Author: L. Mahadevan
E-mail: lmahadev@g.harvard.edu

This PDF file includes:

1. Supplementary Movies

MovieS1 Time evolution movie associated with Fig. 1b.
MovieS2 PIV velocity field of the wild-type chick embryo overlaid over the experimental fluorescence images of the epiblast surface.
MovieS3 Time evolution movie associated with Fig. 3a for different T. The lower panels show the averaged velocity field, the evolution of a dense set of points, and the deformation of an initially uniform grid that moves with the flow.
MovieS4 Time evolution movie associated with Fig. 3d for different T.
MovieS5 Time evolution movie associated with Fig. 4a for different T.
MovieS6 Time evolution movie associated with Fig. 4b for different T.
MovieS7 Time evolution movie associated with Fig. 4b for different T along with cell positions in green.
MovieS8 Time evolution movie associated with Fig. 4c for different T.
MovieS9 Time evolution movie associated with Fig. 4d for different T along with cell positions in green.
MovieS10 Velocity fields of WT and TWI mutant fly embryos.
MovieS11 Time evolution movie associated with Fig. S5 for different T.
MovieS12 Time evolution movie associated with Fig. S6 for different T.
MovieS13 Time evolution movie associated with Fig. S7 for different T.
MovieS14 Time evolution movie associated with Figs. S8a.
MovieS15 Time evolution movie associated with Figs. S8b.
MovieS16 Time evolution movie associated with Figs. S9.

Supporting Information Text

2. Methods

A. FTLE computation on a flat planar domain. We recall fom the main text (Eq. (2)), that the FTLE is defined as

$$FTLE^t_{t_0}(\mathbf{x}_0) = \frac{1}{|T|}\ln\left(\max_{\delta\mathbf{x}_0}\frac{|\overbrace{\nabla\mathbf{F}^t_{t_0}(\mathbf{x}_0)\delta\mathbf{x}_0}^{\delta\mathbf{x}_t}|}{|\delta\mathbf{x}_0|}\right) = \frac{1}{2|T|}\ln\left(\lambda_2(\mathbf{x}_0)\right), \quad \mathbf{C}^t_{t_0}(\mathbf{x}_0) = [\nabla\mathbf{F}^t_{t_0}(\mathbf{x}_0)]^\top\nabla\mathbf{F}^t_{t_0}(\mathbf{x}_0), \tag{1}$$

where $\lambda_2(\mathbf{x}_0)$ denotes the highest eigenvalue of the Cauchy–Green strain tensor $\mathbf{C}^t_{t_0}(\mathbf{x}_0)$, and $^\top$ matrix transposition. To compute the FTLE, we first calculate the flow map

$$\mathbf{F}^t_{t_0}(\mathbf{x}_0) = \mathbf{x}_0 + \int_{t_0}^{t}\mathbf{v}(\mathbf{F}^\tau_{t_0}(\mathbf{x}_0),\tau)\,d\tau, \tag{2}$$

which maps initial cell positions $\mathbf{x}_0$ at time t_0 to their time$-t$ position, by integrating the cell velocity field $\mathbf{v}(\mathbf{x},t)$ using the MATLAB built-in Runge-Kutta solver ODE45 with absolute and relative tolerance of 10^{-6}, linear interpolation in space and time, and a uniform grid of initial conditions $16\mu m$ apart from each other in both directions.

Then, denoting the $i-th$ component of the flow map $\mathbf{F}^t_{t_0}(\mathbf{x}_0)$ by $x^i(x^1_0,x^2_0,t_0,t)$, we compute the deformation gradient $\nabla\mathbf{F}^t_{t_0}(\mathbf{x}_0)$ using the finite-difference approximation (1)

$$\nabla\mathbf{F}^t_{t_0}(\mathbf{x}_0) \approx \begin{bmatrix} \frac{x^1(x^1_0+\delta,x^2_0,t_0,t)-x^1(x^1_0-\delta,x^2_0,t_0,t)}{2\delta} & \frac{x^1(x^1_0,x^2_0+\delta,t_0,t)-x^1(x^1_0,x^2_0-\delta,t_0,t)}{2\delta} \\ \frac{x^2(x^1_0+\delta,x^2_0,t_0,t)-x^2(x^1_0-\delta,x^2_0,t_0,t)}{2\delta} & \frac{x^2(x^1_0,x^2_0+\delta,t_0,t)-x^2(x^1_0,x^2_0-\delta,t_0,t)}{2\delta} \end{bmatrix}, \tag{3}$$

where $\delta = 16\mu m$ as the initial conditions' grid spacing. After computing $\nabla\mathbf{F}^t_{t_0}(\mathbf{x}_0)$, we use eq. Eq. (1) for computing the FTLE field.

B. FTLE computation on a curved surface. In the case of the Drosophila melanogaster dataset, the cell velocity field $\frac{d\mathbf{x}}{dt} = \mathbf{v}(\mathbf{x},t) = [u(\mathbf{x},t),v(\mathbf{x},t),w(\mathbf{x},t)]^\top \in \mathbb{R}^3$ is given on approximately 1800 points $\mathbf{x} = [x,y,z]^\top$ lying on the fixed apical embryo surface $\mathcal{S}\subset\mathbb{R}^3$, as illustrated in Fig. S1. We parametrize $\mathcal{S}$ in polar coordinates $\boldsymbol{\theta} = [\theta,\varphi]^\top \in \mathbb{S}^2$ as

$$\boldsymbol{\theta} = \mathbf{g}(\mathbf{x}) = \begin{bmatrix} \arctan\frac{y}{x} \\ \arcsin\frac{z}{\sqrt{x^2+y^2+z^2}} \end{bmatrix}, \quad \mathbf{x} = \mathbf{h}(\boldsymbol{\theta}) = \begin{bmatrix} \rho(\boldsymbol{\theta})\cos\varphi\cos\theta \\ \rho(\boldsymbol{\theta})\cos\varphi\sin\theta \\ \rho(\boldsymbol{\theta})\sin\varphi \end{bmatrix}, \tag{4}$$

where $\rho(\boldsymbol{\theta})$ is a cubic interpolant function that provides the distance of points on the embryo surface from the origin. The parametrization of any surface topologically equivalent to a two-dimensional sphere is known to possess singularities (cf. Eq. (4)). Indeed $\mathbf{g}$ is not defined at the dorsal (D) and ventral (V) poles. Therefore, we define a second parametrization, which has singularities at the anterior (A) and posterior (P) poles. Together, these two charts allow us to parametrize the embryo surface completely.

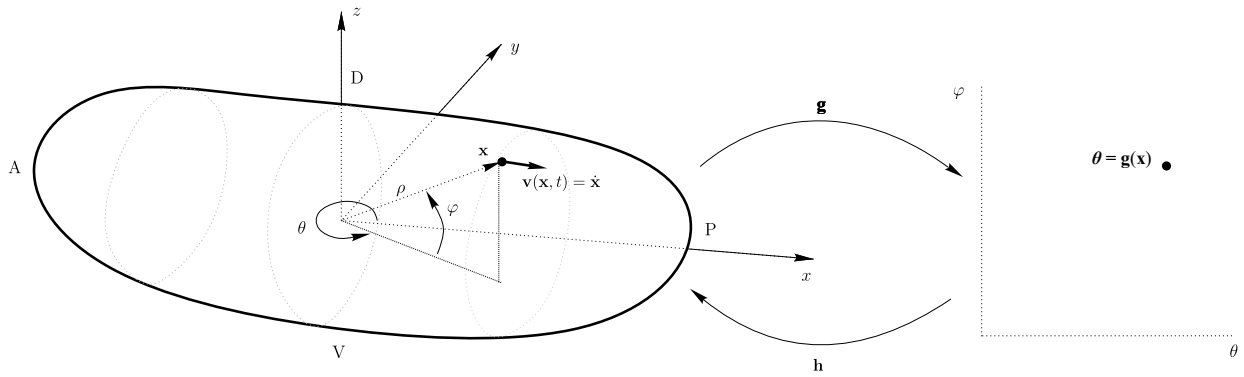

Fig. S1. Polar coordinates $\boldsymbol{\theta} = [\theta, \varphi]^\top \in \mathbb{S}^2$ parametrization of a Drosophila embryo apical surface given as a triangulated set of points $\mathbf{x} = [x, y, z]^\top \in \mathcal{S} \subset \mathbb{R}^3$. The points A,P,D and V mark the locations of the Anterior, Posterior, Dorsal and Ventral poles.

To compute cell trajectories, we have devised an in-house MATLAB code that integrates cell velocities over the triangulated surface using a Runge Kutta 4th order method. We ensure that trajectories remain on $\mathcal{S}$ by projecting current cell positions on $\mathcal{S}$ at each time step. We now define the Lagrangian flow map that maps an initial condition $\mathbf{x}_0$, parametrized by $\boldsymbol{\theta}$, to its final position as

$$\overbrace{\mathbf{F}^t_{t_0}(\mathbf{h}(\boldsymbol{\theta}))}^{\mathbf{x}_t} = \overbrace{\mathbf{h}(\boldsymbol{\theta})}^{\mathbf{x}_0} + \int_{t_0}^{t} \mathbf{v}(\mathbf{F}^\tau_{t_0}(\mathbf{h}(\boldsymbol{\theta})), \tau)\, d\tau. \tag{5}$$

From the Taylor expansion of the Lagrangian flow map with respect to $\boldsymbol{\theta}$, we obtain that

$$\overbrace{\mathbf{F}^t_{t_0}(\mathbf{h}(\boldsymbol{\theta}+\boldsymbol{\delta\theta})) - \mathbf{F}^t_{t_0}(\mathbf{h}(\boldsymbol{\theta}))}^{\delta\mathbf{x}_t} \approx \nabla_{\boldsymbol{\theta}}[\mathbf{F}^t_{t_0}(\mathbf{h}(\boldsymbol{\theta}))]\delta\boldsymbol{\theta}. \tag{6}$$

Using Eqs. (1,6), we rewrite the FTLE in the case of motion on curved surfaces as

$$\begin{aligned} FTLE^t_{t_0}(\boldsymbol{\theta}) =& \frac{1}{|T|}\ln\left(\max_{\delta\boldsymbol{\theta}}\frac{|\nabla_{\boldsymbol{\theta}}[\mathbf{F}^t_{t_0}(\mathbf{h}(\boldsymbol{\theta}))]\delta\boldsymbol{\theta}|}{|\nabla_{\boldsymbol{\theta}}\mathbf{h}(\boldsymbol{\theta})\delta\boldsymbol{\theta}|}\right) \\ =& \frac{1}{|T|}\ln\left(\max_{\delta\boldsymbol{\theta}}\sqrt{\frac{\langle\delta\boldsymbol{\theta}, (\nabla_{\boldsymbol{\theta}}[\mathbf{F}^t_{t_0}(\mathbf{h}(\boldsymbol{\theta}))])^\top(\nabla_{\boldsymbol{\theta}}[\mathbf{F}^t_{t_0}(\mathbf{h}(\boldsymbol{\theta}))])\delta\boldsymbol{\theta}\rangle}{\langle\delta\boldsymbol{\theta}, [\nabla_{\boldsymbol{\theta}}\mathbf{h}(\boldsymbol{\theta})]^\top[\nabla_{\boldsymbol{\theta}}\mathbf{h}(\boldsymbol{\theta})]\delta\boldsymbol{\theta}\rangle}}\right), \end{aligned} \tag{7}$$

where $\langle,\rangle$ denotes the dot product. Using the relations in Eq. (5), we note that $\nabla_{\boldsymbol{\theta}}[\mathbf{F}^t_{t_0}(\mathbf{h}(\boldsymbol{\theta}))]$ is simply the Jacobian of the 3D Flow map, whose $i-th$ component is $x^i(\varphi, \theta, t_0, t)$, with respect to $\boldsymbol{\theta} = [\varphi, \theta]$, and hence can be computed by finite differencing as described in Eq. (3). Similarly, $[\nabla_{\boldsymbol{\theta}}\mathbf{h}(\boldsymbol{\theta})]$ is the Jacobian of the 3D Flow map evaluated at $t = t_0$ with respect to $\boldsymbol{\theta}$, and can be computed either as in Eq. (3) or by explicitly using the form of the parametrization in Eq. (4) as

$$\nabla_{\boldsymbol{\theta}}\mathbf{h}(\boldsymbol{\theta}) = \begin{bmatrix} \partial_\theta\rho(\boldsymbol{\theta})\cos\varphi\cos\theta - \rho(\boldsymbol{\theta})\cos\varphi\sin\theta & \partial_\varphi\rho(\boldsymbol{\theta})\cos\varphi\cos\theta - \rho(\boldsymbol{\theta})\sin\varphi\cos\theta \\ \partial_\theta\rho(\boldsymbol{\theta})\cos\varphi\sin\theta + \rho(\boldsymbol{\theta})\cos\varphi\cos\theta & \partial_\varphi\rho(\boldsymbol{\theta})\cos\varphi\sin\theta - \rho(\boldsymbol{\theta})\sin\varphi\sin\theta \\ \partial_\theta\rho(\boldsymbol{\theta})\sin\varphi & \partial_\varphi\rho(\boldsymbol{\theta})\sin\varphi + \rho(\boldsymbol{\theta})\cos\varphi \end{bmatrix}, \tag{8}$$

where $\partial_\varphi\rho(\boldsymbol{\theta}), \partial_\theta\rho(\boldsymbol{\theta})$ need to be computed by finite differencing. The symmetric tensor $\mathbf{G}(\boldsymbol{\theta}) = [\nabla_{\boldsymbol{\theta}}\mathbf{h}(\boldsymbol{\theta})]^\top[\nabla_{\boldsymbol{\theta}}\mathbf{h}(\boldsymbol{\theta})]$ is the metric tensor of the embryo surface at point $\mathbf{h}(\boldsymbol{\theta})$. We illustrate Eqs. (5-7) in Fig. S2.

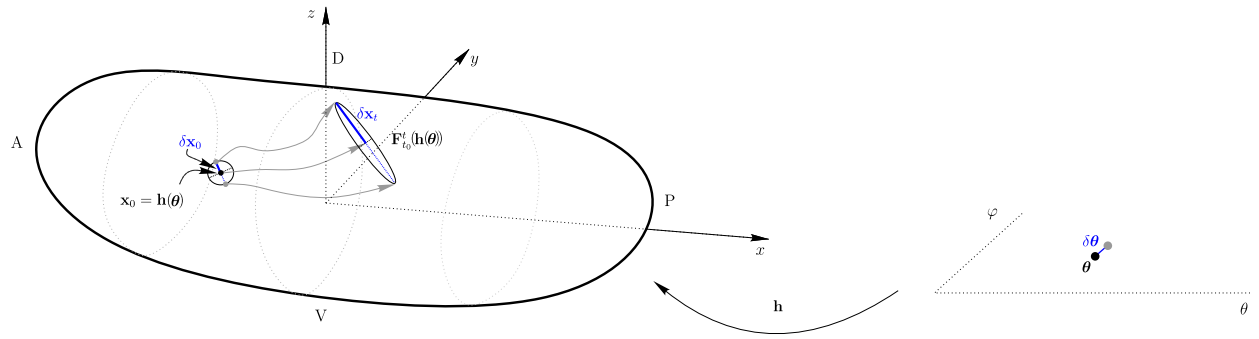

Fig. S2. Time evolution of the relative position vector $\delta\mathbf{x}_t$ between two initially close cells on the embryo surface as a function of polar coordinates (cf. Eqs. (5-6)).

In our analysis, we define a uniform grid of initial conditions $\boldsymbol{\theta}$ spaced by 1 $deg.$, compute 3D trajectories as described above, and the Jacobian matrices in Eq. (7) using finite differencing with step size $\delta = 1deg.$. Finally, we parameterize $\delta\boldsymbol{\theta} = [\cos\alpha, \sin\alpha]^\top$ and compute Eq. (7) numerically using a vector of possible α from 0 to 2π spaced by $1deg.$.

C. Eulerian and Lagrangian assessment of tissue deformations. We recall a known relation (see e.g. (2) for derivation) between the Eulerian rate of strain tensor, broadly used for studying deformations in morphogenesis, and the Lagrangian Cauchy-Green tensor.

$$\sqrt{\frac{\langle \delta\mathbf{x}_0, \mathbf{C}_{t_0}^t(\mathbf{x}_0)\delta\mathbf{x}_0\rangle}{\langle \delta\mathbf{x}_0, \delta\mathbf{x}_0\rangle}} = \frac{|\delta\mathbf{x}_t|}{|\delta\mathbf{x}_0|} = \mathrm{Exp}\left[\int_{t_0}^{t} \frac{\langle \nabla\mathbf{F}_{t_0}^\tau(\mathbf{x}_0)\delta\mathbf{x}_0, \mathbf{S}(\mathbf{F}_{t_0}^\tau(\mathbf{x}_0),\tau)\nabla\mathbf{F}_{t_0}^\tau(\mathbf{x}_0)\delta\mathbf{x}_0\rangle}{\langle \nabla\mathbf{F}_{t_0}^\tau(\mathbf{x}_0)\delta\mathbf{x}_0, \nabla\mathbf{F}_{t_0}^\tau(\mathbf{x}_0)\delta\mathbf{x}_0\rangle} d\tau\right] \quad [9]$$

To gain a better intuition of the differences between an Eulerian assessment of deformation encoded in $\mathbf{S}$, and the corresponding Lagrangian (i.e. with memory) one, we consider two velocity fields one multiple of each other $\tilde{\mathbf{v}}(\mathbf{x},t) = c\mathbf{v}(\mathbf{x},t)$. The corresponding rate of strain tensors are related by $\tilde{\mathbf{S}}(\mathbf{x},t) = c\mathbf{S}(\mathbf{x},t)$, hence having the same eigenvectors and topology of the eigenvalues. By contrast, the Lagrangian deformation encoded in $\mathbf{C}_{t_0}^t(\mathbf{x}_0)$ will have different spatial structures for a fix $[t_0, t]$ in these two systems because cell paths in the modified flow $\tilde{\mathbf{F}}_{t_0}^t(\mathbf{x}_0) = \mathbf{x}_0 + c\int_{t_0}^t \mathbf{v}(\tilde{\mathbf{F}}_{t_0}^\tau(\mathbf{x}_0),\tau)\, d\tau$ will visit different points compared to the original one (Eq. (2)). A similar reason holds for the associated deformation gradient $\tilde{\nabla}\tilde{\mathbf{F}}_{t_0}^t(\mathbf{x}_0) = \mathbf{I} + c\int_{t_0}^t \nabla\mathbf{v}(\tilde{\mathbf{F}}_{t_0}^\tau(\mathbf{x}_0),\tau)\tilde{\nabla}\tilde{\mathbf{F}}_{t_0}^\tau(\mathbf{x}_0)\, d\tau$. These simple relations highlight that both uniform as well as localized changes of tissue flows can lead to global changes, which can be detected by Lagrangian methods while remaining inaccessible to Eulerian ones.

D. Isotropic and anisotropic contribution to Lagrangian attraction. We recall that attracting LCSs, captured by the backward FTLE, can occur because of isotropic contraction or anisotropic deformation, as described in the main text. We denote by $|\delta\mathbf{x}_t^\top| = |\delta\mathbf{x}_0| + \Delta^I + \Delta^A$ the final distance of two particles initially distant $|\delta\mathbf{x}_0|$, where Δ^I, Δ^A denote the distance change due to isotropic and anisotropic deformations. The isotropic area shrinkage induced by $\mathbf{F}_{t_0}^t(\mathbf{x}_0)$ on an infinitesimal patch centered at $\mathbf{x}_0$ can be computed as

$$\frac{A_t(\mathbf{x}_0)}{A_0(\mathbf{x}_0)} = \sqrt{\det \mathbf{C}_{t_0}^t(\mathbf{x}_0)}, \quad t < t_0, \quad [10]$$

and induces particle convergence in forward time, as illustrated and quantified in Fig. S3 (Center). This scalar field is based at the final configuration $\mathbf{x}_0$ and integrates information over the time interval $[t, t_0]$. It attains values greater than unity in regions where initially far trajectories converge because of isotropic contraction, and is less than unity in regions where initially close trajectories diverge due to isotropic expansion. We compute the convergence due to anisotropic deformation as the total convergence minus the one from isotropic shrinkage (Fig. S3 Right). Using the expressions in Fig. S3, we define the percentage

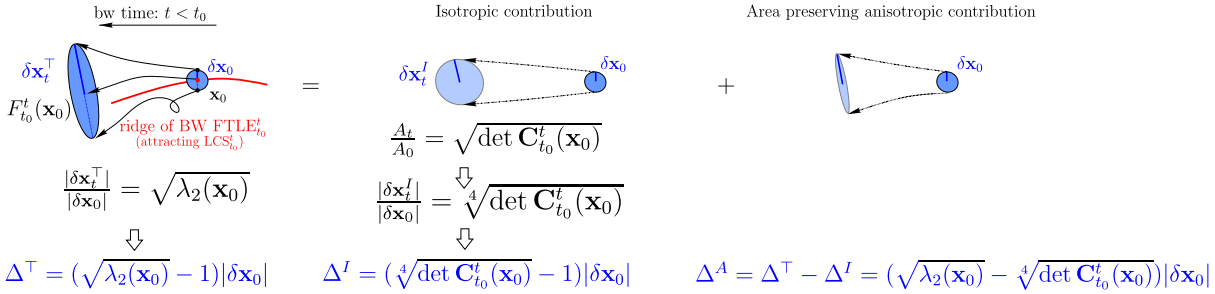

Fig. S3. (Left) Backward FTLE ridge as in Fig. 2b. The BW FTLE is a rescaled form of the maximum convergence achieved by two initially distant particles in forward time. (Center) Particles convergence induced by isotropic area contraction quantified by eq. Eq. (10). (Right) Particles convergence due to area preserving anisotropic deformation.

of Lagrangian attraction due to anisotropic deformation as

$$\%An.Def._{t_0}^t(\mathbf{x}_0) = \frac{\Delta^A}{|\Delta^I| + \Delta^A}\% = \left(\frac{\sqrt{\lambda_2(\mathbf{x}_0)} - \sqrt[4]{\det \mathbf{C}_{t_0}^t(\mathbf{x}_0)}}{|\sqrt[4]{\det \mathbf{C}_{t_0}^t(\mathbf{x}_0)} - 1| + \sqrt{\lambda_2(\mathbf{x}_0)} - \sqrt[4]{\det \mathbf{C}_{t_0}^t(\mathbf{x}_0)}}\right) 100, \quad t < t_0, \quad [11]$$

which completely characterize the Lagrangian cell convergence. Because $\det \mathbf{C}_{t_0}^t(\mathbf{x}_0) = \lambda_1(\mathbf{x}_0)\lambda_2(\mathbf{x}_0)$ and $\lambda_1(\mathbf{x}_0) \leq \lambda_2(\mathbf{x}_0)$ by definition, it follows that $\Delta^A \geq 0$. Note that if the cell velocity field is incompressible ($\nabla\cdot\mathbf{v} = 0$), by Liouville's formula (3) $\det \mathbf{C}_{t_0}^t(\mathbf{x}_0) = 1$, and $\%An.Def._{t_0}^t(\mathbf{x}_0) = 100$ as all the attraction is caused by anisotropic deformations. Conversely, if anisotropic deformations are absent, an initially circular patch remains circular, hence the two eigenvalues of $\mathbf{C}_{t_0}^t(\mathbf{x}_0)$ characterizing the deformed ellipse semi axes are identical $\lambda_2(\mathbf{x}_0) = \lambda_1(\mathbf{x}_0) = \lambda(\mathbf{x}_0)$. Therefore, it follows that $\sqrt[4]{\det \mathbf{C}_{t_0}^t(\mathbf{x}_0)} = \sqrt[4]{\lambda_2(\mathbf{x}_0)\lambda_1(\mathbf{x}_0)} = \sqrt[4]{\lambda^2(\mathbf{x}_0)} = \sqrt{\lambda(\mathbf{x}_0)}$, which makes $\%An.Def._{t_0}^t(\mathbf{x}_0) = 0$, as desired.

3. Chordin and Wnt8C expression patterns during primitive streak formation in chicken embryo

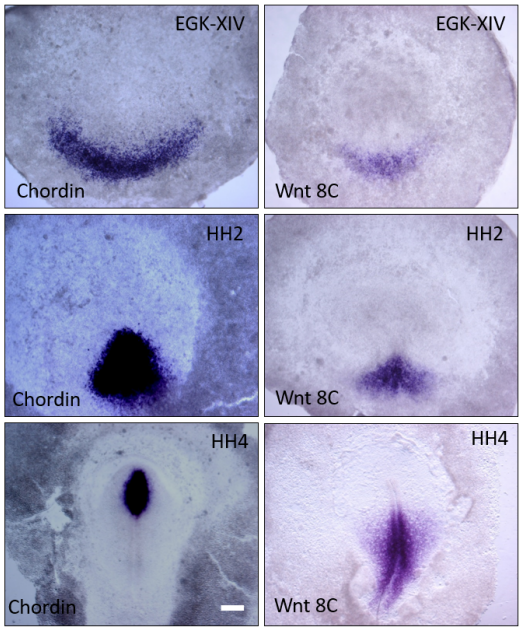

Fig. S4. Chordin and Wnt8C expression patterns in pre and gastrulation stage chick embryos. Embryos were fixed at different stages (EGK-XIII, HH2 and HH4) of development and RNA expression detected using standard in-situ hybridisation procedures (4). Both Chordin and Wnt8c are initially expressed in a sickle shape region in the posterior chick epiblast, followed by their separation during streak extension. Chordin is expressed in the anterior streak, while Wnt8c is expressed in the posterior streak and the mesoderm cells that migrate from out of the posterior streak. White scale bar 0.5mm.

4. Lagrangian deformation types behind primitive streak formation in chicken embryo

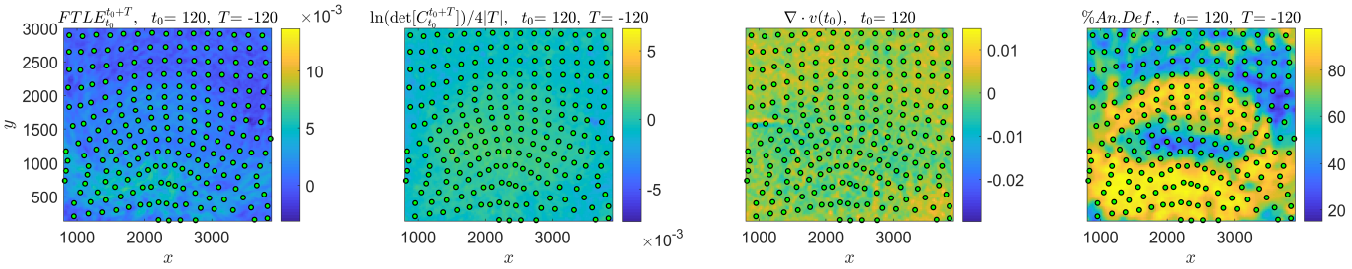

Fig. S5. (First) BW FTLE of the wild-type chick embryo corresponding to $|T| = 2h$ shortly after egg laying (stage EKG XII), whose high values demarcates the forming PS. (Second) Isotropic Lagrangian attraction field (quantified Fig. S3 Center) rescaled by the logarithm and normalized by $|T|$, as in the FTLE definition. (Third) Eulerian velocity field divergence. The first three scalar fields are in min^{-1}. (Fourth) $\%An.Def._{t_0}^{t}(\mathbf{x}_0)$ field defined in Eq. (11). Movie S11 shows the full evolution of the above scalar fields for different T, along with cells position (green).

The first panel of Fig. S5 shows the BW FTLE and cell positions corresponding to $|T| = 2h$ for the chick wild-type embryo analyzed in Fig. 3(a). The second panel shows the Lagrangian Isotropic attraction rescaled by the logarithm and normalized by $|T|$, as in the FTLE definition. The high BWFTLE value region, capturing the forming PS, is completely hidden in the Isotropic attraction field, which attains higher values in the middle of the domain. The forming PS is also completely hidden to the velocity divergence field (third panel), which is the instantaneous version ($T \to 0$) of the Lagrangian area shrinkage in the second panel, and whose negative values demarcate regions characterized by instantaneous isotropic contraction. The right panel shows the $\%An.Def.$ field defined in eq. Eq. (11) highlighting that the high BW FTLE region in the First panel is mainly ($\geq 80\%$) due to anisotropic deformation. Movie S11 shows the time evolution of Fig. S5 for different T, and indicates that cell convergence giving rise to the PS is always dominated by anisotropic tissue deformation.

5. Morphogenetic features extraction from the FTLE field

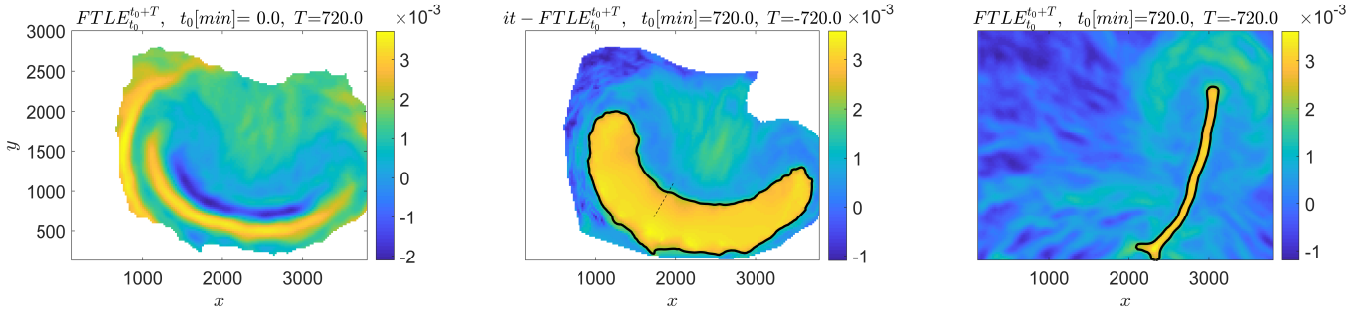

Fig. S6. Same scalar fields as in Fig. 3(a) smoothed with an average filter of window size 3x3. (Left) FW FTLE field. (Center) BWFTLE passively transported at the initial time. The solid black line is a level set of the BWFTLE field delimiting the area of cells that will form the PS at their initial positions. The level set value is automatically selected evaluating the BWFTLE along the dashed black segment (from bottom to top) and detecting the value at which the derivative is minimal. (Right) BWFTLE based at the final time. The solid black curve is the BWFTLE level set corresponding to the value identified in the center panel. Movie S12 shows the full evolution of the above scalar fields for different T. We compute the area enclosed by the black solid line in the center panel by using an in-built MATLAB function.

6. Dynamic Morphoskeletons behind primitive streak formation in chicken embryo using unfiltered velocity data

While filtering velocities is necessary for Eulerian methods, owing to their sensitivity to noise and measurement errors, it may hide finer-scale structures whose characteristic sizes are smaller than the filtering window sizes. By contrast, Lagrangian methods are intrinsically more robust because the integration of cell velocities along trajectories acts like a filter.

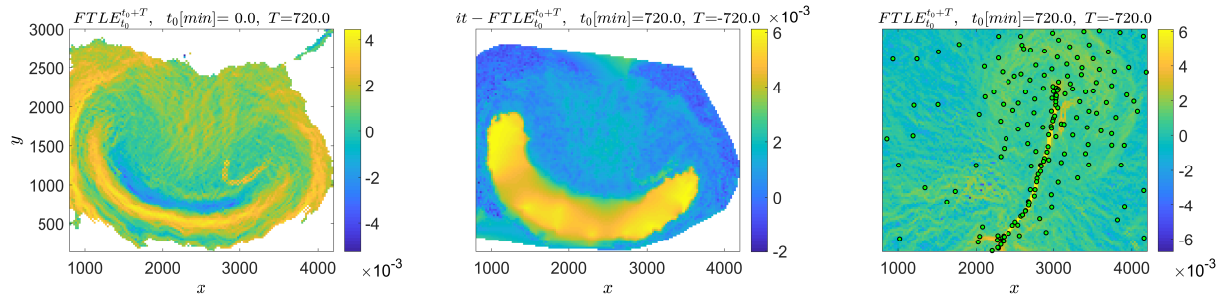

Fig. S7. Same scalar fields as in Fig 3a, computed from raw (unfiltered) velocity data. (Left) FW FTLE corresponding to the full extent of the dataset ($|T| = 12h$ from the freshly laid egg stage), whose high values demarcates two repelling LCSs as described in in Fig 3a. (Right) BW FTLE corresponding to the full extent of the dataset whose strong ridge highlights the attracting LCS corresponding to the formed PS. Cells position at $12h$, initialized from a uniform gird at $0h$, are shown by green dots. White areas correspond to regions where the FTLE is unavailable because trajectories left the domain over which the velocity field is defined. (Center) BW FTLE shown in (Right) passively transported by F_{720}^{0} shows the initial cell positions that will finally form the PS. The FTLE has unit $\mathrm{min}^{-}1$, the axis units are in μm and the posterior anterior direction goes from smaller to larger y values. Movie S13 shows the full time evolution of BW and FW FTLE for different T, along with cells position.

7. Drosophila Melanogaster WT: dorsal and posterior pole repellers

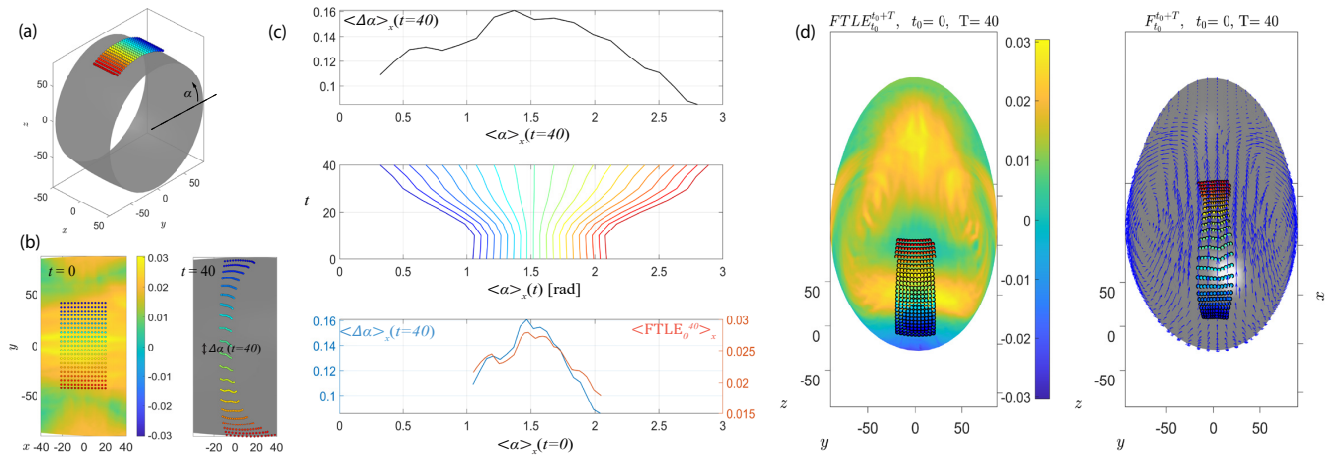

Fig. S8. (a-c) Dorsal repeller in the WT drosophila dataset illustrated in Figs. 4a,e. (a) Initial cell positions placed across the dorsal repeller color-coded by increasing values of α. (b) Left: dorsal view of the initial cell positions shown in (a) along with the corresponding FTLE_0^{40} field encoded in the colorbar. Right: final cell positions. Movie S14 shows cell positions over time. (c) Center: Kymograph of $x-$averaged angular position $< \alpha >_x (t)$ for the color-coded rows of points shown in (a,b). Top: $x-$averaged angular distance $< \Delta\alpha >_x (t = 40)$ between consecutive rows of points (see panel b) graphed over $< \alpha >_x (t = 40)$. Bottom: $x-$averaged angular distance (blue) between consecutive rows of points graphed over $< \alpha >_x (t = 0)$. The red curve shows the $x-$averaged FTLE_0^{40} in correspondence of the initial grid of cells (panel b) for different values of α. (d) Same analysis of (b) for the posterior pole repeller in the WT drosophila dataset shown in Fig. 4a along with cell velocity field in blue. Movie S15 shows the time evolution of cell positions and velocities. The FTLE has unit $\min^-1$, and the Cartesian axis units are in μm.

Figures S8a-c illustrate the influence of the dorsal repeller in the WT drosophila dataset (cf. Figs. 4a,e). We place a set of cells across the dorsal repeller color-coded by increasing values of α (a). We show the initial and final cell positions in (b) along with a movie with intermediate time steps (Movie S14). The scalar field in the left panel encodes FTLE_0^{40}. Using a kymograph, we plot the tissue deformation across the repeller in (c) center. For each color-coded row of points, we compute the $x-$averaged angular position $< \alpha >_x (t)$. In the top panel, we show the $x-$averaged angular distance $< \Delta\alpha >_x (t = 40)$ between consecutive rows of points (see panel b) graphed over $< \alpha >_x (t = 40)$. We graph the same quantity in the bottom panel over $< \alpha >_x (t = 0)$ (blue curve) along with the $x-$averaged FTLE_0^{40} (red curve) in correspondence of the initial grid of cells (panel b) for different values of α. Although the FTLE ridge is diffuse, peaks of $< \text{FTLE}_0^{40} >_x$ accurately predict embryo regions that will undergo the highest stretching. To check tissue deformations from the FTLE, we note that for $\alpha \approx \pi/2$, $< \text{FTLE}_0^{40} >_x \approx 0.027$, which implies a stretching $\sqrt{\lambda_2} \approx 2.9$. For the rows of points starting at $\alpha \approx \pi/2$, $< \Delta\alpha >_x (t = 40) \approx 0.15$. Assuming only deformation along α, from the relative displacement of cells $\sqrt{\lambda_2} \approx \frac{R\Delta\alpha(t=40)}{R\Delta\alpha(t=0)} = \frac{0.15}{3\pi/180} \approx 2.9$, where we used that $R \approx 50\mu m$ (panel a) remains constant between initial and final cell positions, and that the initial α spacing of cell rows is 3 $deg.$. This confirms that the FWFTLE marks regions of distinct repulsion as well as quantifies areas of maximum tissue deformation over a desired T. This characterization, by contrast, remains hidden to Eulerian methods and cell trajectory plots.

Figure S8b shows the same analysis of panel (b) for the posterior pole repeller in the WT drosophila dataset shown in Fig. 4a along with the cell velocity field in blue. During GBE, the repeller highlights the precise region of distinct cell separation (and tissue deformation), which is confirmed by the relative motion of color-coded cells. Specifically, the color-coded rows of cells that start within the repeller undergo visibly higher separation compared to the nearby rows. Movie S15 shows the corresponding time evolution of cell positions, further illustrating that the Lagrangian repeller is inaccessible to Eulerian velocity plots.

8. Drosophila Melanogaster TWI: ventral repellers

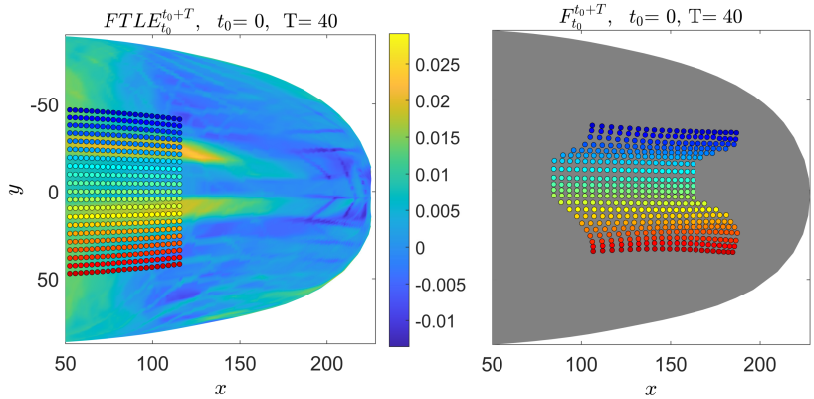

Fig. S9. Left: FWFTLE$_0^{40}$ shows two ventral repellers in the TWI drosophila dataset. Dots indicate initial cell positions color-coded for increasing values of α, as in Fig. S8a. Right: final cell positions confirm that cells across the repellers undergo high separation induced by shear deformations. Movie S16 shows cell positions over time. The FTLE has unit $\mathrm{min}^-\ 1$, and the Cartesian axis units are in μm.

References

1. Haller G (2001) Distinguished material surfaces and coherent structures in three-dimensional fluid flows. *Physica D* 149(4):248–277.
2. Serra M, Vétel J, Haller G (2018) Exact theory of material spike formation in flow separation. *J. Fluid Mech.* 845:51–92.
3. Guckenheimer J, Holmes P (1983) *Nonlinear oscillations, dynamical systems, and bifurcations of vector fields*. (Springer Science & Business Media) Vol. 42.
4. Wilkinson DG, Nieto MA (1993) [22] detection of messenger rna by in situ hybridization to tissue sections and whole mounts in *Methods in enzymology*. (Elsevier) Vol. 225, pp. 361–373.